Multiple Zonal Jets in a Differentially Heated Rotating Annulus*,+

CARLOWEN A. SMITH AND KEVIN G. SPEER

Geophysical Fluid Dynamics Institute and Department of Earth, Ocean, and Atmospheric Science, Florida State University, Tallahassee, Florida

ROSS W. GRIFFITHS

Research School of Earth Sciences, Australian National University, Canberra, Australia

(Manuscript received 22 November 2013, in final form 3 June 2014)

ABSTRACT

A laboratory experiment of multiple baroclinic zonal jets is described, thought to be dynamically similar to flow observed in the Antarctic Circumpolar Current. Differential heating sets the overall temperature difference and drives unstable baroclinic flow, but the circulation is free to determine its own structure and local stratification; experiments were run to a stationary state and extend the dynamical regime of previous experiments. A topographic analog to the planetary β effect is imposed by the gradient of fluid depth with radius supplied by a sloping bottom and a parabolic free surface. New regimes of a low thermal Rossby number ($\mathrm{Ro}_T \sim 10^{-3}$) and high Taylor number ($\mathrm{Ta} \sim 10^{11}$) are explored such that the deformation radius L_ρ is much smaller than the annulus gap width L and similar to the Rhines length. Multiple jets emerge in rough proportion to the smallness of the Rhines scale, relatively insensitive to the Taylor number; a regime diagram taking the β effect into account better reflects the emergence of the jets. Eddy momentum fluxes are consistent with an active role in maintaining the jets, and jet development appears to follow the Vallis and Maltrud phenomenology of anisotropic wave–turbulence interaction on a β plane. Intermittency and episodes of coherent meridional jet migration occur, especially during spinup.

1. Introduction

In the Southern Ocean, the air–sea buoyancy flux acts together with the wind stress to create the Antarctic Circumpolar Current (ACC). This current flows essentially in geostrophic balance with the meridional density gradient set by the freezing temperatures near Antarctica and the warm subtropical gyres. The ACC is not a single front but a complex system of fronts, several of which are thought to be of circumpolar extent (Orsi et al. 1995). Two principal fronts typically carry a large fraction of the transport of the ACC, the Subantarctic Front (SAF) and the Polar Front (PF; e.g., Cunningham et al. 2003), but other fronts can have comparable transports in individual hydrographic sections. Numerous zonal jets in the ACC were dramatically resolved in the study of Sokolov and Rintoul (2007, 2009). Observational evidence is also growing that not only the ACC, but much of the deep ocean flow is permeated by zonal jets (Nakano and Suginohara 2002; Treguier et al. 2003; Herbei et al. 2008).

The study of the development of quasi-zonal jets in geophysical contexts has an extensive background. Panetta (1993) examined the emergence of such jets over long time scales in numerical simulations and emphasized the need for large-scale forcing, so that the flow itself determines the scales of interaction. Treguier and Panetta (1994) examined these ideas in the context of a model of the ACC and found multiple jets; large-scale

* Supplemental information related to this paper is available at the Journals Online website: http://dx.doi.org/10.1175/JPO-D-13-0255.s1.

+ Geophysical Fluid Dynamics Institute Contribution Number 469.

Corresponding author address: Carlowen A. Smith, Department of Earth, Ocean, and Atmospheric Sciences, Geophysical Fluid Dynamics Institute, Florida State University, 018 Keen Building, 77 Chieftain Way, Tallahassee, FL 32306-4360.
E-mail: csmith@gfdi.fsu.edu

DOI: 10.1175/JPO-D-13-0255.1

topography was found to create regions of enhanced kinetic energy (mean and eddy), while the circumpolar continuity of these jets was thought to be due to transient eddies. Some laboratory studies of jets are reviewed by Rhines (1994), including the dynamics and transport of Rossby waves and jets explored by, for example, Sommeria et al. (1989) and Sommeria (1991). Recent progress in the research on multiple jets was presented in a special collection for jets and annular structures in geophysical fluids (*Journal of Atmospheric Sciences*, available online at http://journals.ametsoc.org/page/Jets).

Numerical modeling has pointed to the emergence of multiple jets as an intrinsic part of the dynamics of planetary-scale circumpolar flow (Williams 1978; Panetta 1993; Treguier and Panetta 1994; Galperin et al. 2004). However, frontal dynamics are not well resolved in basin-scale geometries without restricting the domain size or dynamics (e.g., quasigeostrophic dynamics; Treguier et al. 2003; Galperin et al. 2004). In these higher-resolution models the Rhines (1975) scale,

$$L_R \equiv \sqrt{U/\beta}, \tag{1}$$

where U is a characteristic eddy velocity and β is the planetary vorticity gradient, is thought to play a fundamental role in setting the meridional scale of the jets. The presence of a topographic β can play an analogous role in setting this scale (e.g., Sinha and Richards 1999).

Recent research (Mcintyre 2008; Sukoriansky et al. 2007) has raised the issue of the physical meaning of the Rhines scale and whether the Rhines scale is the appropriate scaling for jet spacing. In decaying quasi-2D turbulence with a β effect, the Rhines scale represents the jet spacing and the initial scale at which the inverse cascade is arrested and the turbulence and wave regimes are separated (Rhines 1975). However, the coincidence of the Rhines scale with the jet spacing in the zonal jet regime might reflect a lack of scale separation from the dominant (large) scale of friction (Sukoriansky et al. 2007).

In a recent differentially heated rotating annulus experiment (Wordsworth et al. 2008), the jet width is found to be much larger than the originally defined Rhines scale; Bastin and Read (1998) similarly find difficulties using the Rhines scale. Condie and Rhines (1994) describe multiple jets over sloping topography that scale with the deformation radius. Slavin and Afanasyev (2012) develop a modified Rhines scale to explain their results, while Berloff et al. (2009) found in an idealized quasigeostrophic (QG) zonal channel model that the Rhines scale is not consistent with the modeled meridional jet spacing.

Instability of the large-scale flow associated with the meridional density gradient generates baroclinic eddies. However, nonlinear baroclinic interactions alone can only transfer energy to smaller scales and cannot participate in an inverse energy cascade by themselves. Eddy kinetic energy (EKE) generated near the deformation radius scale L_D by baroclinic instability is transferred by nonlinear interactions into the barotropic mode (Smith and Vallis 2001). Energy then can follow the inverse energy cascade to larger and larger scales. Beyond the Rhines scale, wave dynamics dominate and energy transfer occurs less from eddy–eddy interactions and more from wave triad interactions (Salmon 1998; Read 2001).

The assumption that barotropization is rapid relative to other processes has led to a host of laboratory (Afanasyev and Wells 2005; Afanasyev and Craig 2013; Di Nitto et al. 2013a,b; and references therein) and numerical (e.g., Dritschel and Scott 2011; Scott and Tissier 2012; Scott and Dritschel 2012) studies that focus on 2D turbulence with stochastic forcing at a given scale, representing the injection of barotropic energy at L_D. This work has established an alternate formulation of the Rhines parameter (e.g., Scott and Dritschel 2012; and references therein):

$$k_{\beta,\varepsilon} \equiv (\beta^3/\varepsilon)^{1/5}, \tag{2}$$

where ε is the rate of energy injection into turbulent motion (Vallis 2006).

The ACC experiences a variety of eddy-forcing scales, as these emerge from instability in a highly inhomogeneous system. This as well as other baroclinic effects concerning local changes in stratification, vertical motions around fronts, and the ''baroclinic lifecycle'' (Lappa 2012) have led to interest in simulations of multiple zonal jet formation in baroclinic, geostrophic turbulence. Because of the extreme computational cost, baroclinic simulations (Panetta 1993; Boland et al. 2012) must simplify dynamics and limit resolution or domain size.

In light of these issues, buoyancy-driven laboratory experiments are playing an important role in our understanding of the large-scale circulation in these highly turbulent and inherently nonlinear regimes (Read 2001; Read et al. 2004, 2007; Wordsworth et al. 2008; Wordsworth 2009). Read's thorough review (Read 2001) places experiments into two categories: those that are continuously forced throughout and those where the spindown of an initial state is observed. These categories are further subdivided into experiments that examine the turbulence resulting from the breakup of a flow forced at large scales and the turbulence that results

from the direct forcing of baroclinic eddies of a specific size.

Effectively resolving the dynamics of the forward and inverse energy cascade in a baroclinic laboratory experiment requires a large separation between the scales of instability L_D and domain-scale L:

$$L_D/L \ll 1. \tag{3}$$

Similarly,

$$L_R/L \ll 1 \tag{4}$$

is needed so that an ''arrest'' of the inverse energy cascade may be observed.

This first requirement [Eq. (3)] was explored by Read and collaborators (Read et al. 2004, 2007), who performed experiments on a very large scale. They used the 13-m diameter Coriolis table at Grenoble to construct an effective working gap of 4.5 m in which multiple jets were able to develop. In this experiment, small eddying motion was induced by spraying a thin, convectively unstable layer of saltwater on the surface of the working fluid. This created an essentially barotropic and homogeneous eddy field, as the convective time scale of the chimneys was much faster than the evolution of the large-scale flow. The addition of a topographic β plane permitted jets to form, accompanied by a peak in the zonal wavenumber spectrum near the Rhines scale. The dramatic results of this experiment confirmed that small-scale motions can be a major driving mechanism for the formation of large-scale zonal jets in a very low Ekman number regime. However, only a relatively limited number of rotation periods could be observed, during which the stratification slowly built up, leading to questions about whether or not a stationary state had been reached.

Zhang and Afanasyev (2014) also observed jets produced in a barotropic flow with a topographic β effect. Forced by inertial eddies created through the electromagnetic Lorentz forcing of the fluid (Afanasyev and Wells 2005), the experiment could be observed for a much longer time, albeit in a much smaller ($\approx$1 m) domain.

Zhang and Afanasyev (2014) and Slavin and Afanasyev (2012) also conducted baroclinic experiments in the presence of a β effect, although in a slightly different context than that conducted here. Their experiments were of an initially homogeneous fluid that was heated from below along a meridional strip. This produced localized convective instabilities that propagated zonally throughout the fluid. These experiments isolate the vital role that β plumes' dynamics play in the formation of zonal structures, but they do not provide for eddy forcing that evolves with the large-scale flow.

Several key aspects of the problem, continuous forcing, ability to equilibrate over long periods of time, and eddies emerging freely from the flow, can be achieved in a differentially heated, rotating annulus of fluid. In this setup, a large-scale density gradient is maintained by temperature forcing across a zonally reentrant channel (see schematic in Fig. 3 below). In turbulent regimes, multiple fronts appear that seem to show dynamic similarity to the jets in the ACC.

''Classic'' annulus experiments (with no β effect) provided us with the basic regime diagram that guides thinking to this day, with a flow governed by two dimensionless parameters (Hide 1958), the Taylor number,

$$\mathrm{Ta} \equiv \frac{4\Omega^2 L^5}{\nu^2 d}, \tag{5}$$

and the thermal Rossby number,

$$\mathrm{Ro}_T \equiv \frac{g\alpha \Delta T d}{\Omega^2 L^2}, \tag{6}$$

where Ω is the rotation rate of the table, L is the annulus gap width, ν is the kinematic viscosity, d is the fluid depth, g is the acceleration of gravity, α is the linear thermal expansion coefficient, and ΔT is the temperature difference applied across the annulus gap.

As Ro_T decreases and Ta increases, the flow in the annulus transitions from an axisymmetric ''Hadley'' overturning regime, to a Rossby-like wave regime, to unstable ''vacillating'' wave modes, to full geostrophic turbulence (Fig. 1). The experimental domain size in the classic annulus experiments would typically not be much larger than the deformation radius ($L_D/L \sim 1$), which prevented the transition to regimes relevant to the ocean.

While this was sufficient for studying midlatitude terrestrial atmospheric turbulence, the requirements for multiple zonal jets necessitates pushing the classical apparatus into a much more turbulent regime.

Furthermore, the β effect was typically neglected in the classic annulus experiments (White 2010). A notable exception is the work of Mason (1975), who conducted annulus experiments with a topographic β effect imposed by a radial depth gradient. This was achieved with a rigid top/bottom with a radial slope. Mason used point measurements of temperature to identify changes in jet structure, different regime transitions, and the existence of a two-jet regime at high Ω values. More recently, Wordsworth (2009) observed full velocity fields of

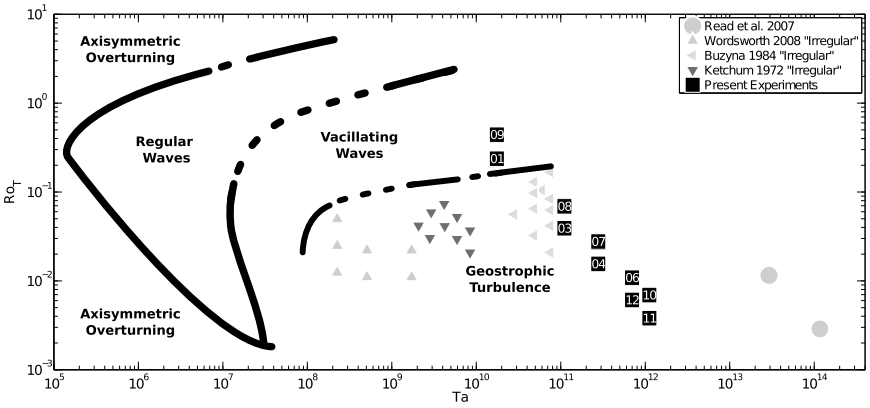

FIG. 1. Thermal Rossby vs Taylor number regime space. The classical annulus regime transition boundaries identified by Hide and Mason (1970), Ketchum (1972), Mason (1975), Buzyna et al. (1984), and Hignett et al. (1985) are shown as solid black lines. The present experiments (numbered black boxes) are shown relative to the salt-forced Grenoble experiment (Read et al. 2007) and previous thermal annulus experiments in the turbulent regime (Ketchum 1972; Wordsworth et al. 2008). Only turbulent or irregular annulus cases are plotted. Note the apparent insensitivity of regime on Ta for Ta $\gtrsim 10^8$ for experiments of varying dimension and Prandtl number.

multiple jet flow in an annulus and was able to quantify eddy mean–flow interaction and unambiguously demonstrate nonlocal spectral transfer (Wordsworth et al. 2008).

It should be noted that although careful control of the depth gradient is desirable, a rigid top may result in the reduction of eddy kinetic energies (suggested by Maher 2010); therefore, we employ only a sloping bottom and a free surface.

We have conducted a series of laboratory experiments to investigate jet formation in a thermally driven system. By using a differentially forced annulus rotated at a higher rate than previous experiments, we extend the dynamical regime to smaller Ro_T and L_R/L. Our laboratory setting provides differential heating that sets the overall ''global'' temperature difference, but the circulation is free to determine its own structure and stratification. We additionally investigate different levels of anisotropy based on the relative strength of thermal forcing and the β effect.

2. Scaling the thermal and β effects

The Taylor number [Eq. (5)] compares the relative effects of viscosity to the Coriolis effect. It takes many forms depending on the context (Lappa 2012, section 1.6.2). The form used here is equivalent to $\mathrm{Ta} = \mathrm{E}^{-2}\delta^{-5}$, where $\mathrm{E} = \nu/(2\Omega d^2)$ is the Ekman number and $\delta = d/L$ is the aspect ratio. This form has traditionally been used in the context of thermal annulus experiments to emphasize the role of the aspect ratio in setting the relative importance of sidewall boundary layers versus internal viscosity in controlling friction (Hide and Mason 1975). Note that some authors (e.g., Pfeffer et al. 1974, 1980a,b; Buzyna et al. 1984) use a different form that is equivalent to E^{-2}.

Determining a representative Taylor number for the ocean is problematic because it requires the identification of an appropriate eddy viscosity in the boundary layers. By comparing the scales of the Ekman layer ($\sim$100 m) to the depth of the ocean ($\sim$4000 m), we can determine the order of the Ekman number to be $\mathrm{E} = d_\mathrm{E}/d \sim 10^{-2}$. The effective viscosity that would be required to achieve this depth would be $\nu_\mathrm{eff} = fd^2 \cdot \mathrm{E} \sim 10^{-2}\,\mathrm{m^2\,s^{-1}}$. Despite this, the large lateral length scale of the ocean puts the Ta $\gtrsim 10^{28}$ at much higher values than any of the laboratory experiments.

In classical annulus experiments, the Taylor number was identified as being most important to the transition between axisymmetric and regular wave flows (Fig. 1). After this transition, it was shown to be relatively unimportant. In Fig. 1, we plot the regimes covered by several annulus experiments along with the reported runs that were termed ''irregular'' or ''chaotic'' (triangles). One can see that, for multiple tank geometries and forcing parameters, the transition seems to occur at a relatively constant value of Ro_T, which does not seem to change with Ta. For this reason, we believe that exact dynamic similarity of Ta between the experiment and the ACC is unimportant above a threshold near Ta $\gtrsim 10^8$.

The thermal Rossby number relates the buoyancy to Coriolis terms and may be written as a Rossby number

[Eq. (6)] using a baroclinic velocity scale U_ρ from the thermal wind:

$$U_\rho = \frac{g\alpha\Delta T d}{2\Omega L}. \tag{7}$$

By using the horizontal ΔT as the scale of the stratification, we can define a length scale L_ρ for the baroclinic deformation radius:

$$L_\rho = \sqrt{\frac{g\alpha\Delta T d}{(2\Omega)^2}}. \tag{8}$$

The thermal Rossby number can then be expressed as a squared ratio of the deformation scale to the gap width:

$$\mathrm{Ro}_T = L_\rho^2/L^2. \tag{9}$$

It should be noted that at high rotation, the isothermal slopes can be quite high, and the local $\partial T/\partial z$ can be much less than the imposed ΔT [see, e.g., the instantaneous temperature fields of Read (1985)]. Even in the case of extreme or outcropping thermal fronts, L_ρ is useful as a controlling parameter of the system and scale for the radius of deformation.

The topographic β effect is imposed by a change in fluid thickness with radius:

$$\beta = \frac{2\Omega}{d}\frac{\partial}{\partial r}(h - h_b) = \frac{2\Omega}{d}s, \tag{10}$$

where s is the (nondimensional) gradient in depth.

Because of different interpretations of the Rhines (1975) mechanism, definitions of the Rhines length other than Eq. (1) exist that are based on the rate of energy input through mechanical forcing (Vallis and Maltrud 1993). Determining this rate is, however, not straightforward in the present experiment. Much of the energy provided through thermal forcing goes into available potential energy through the maintenance of sloping isopycnals and, by definition, the equilibrium state involves no rate of change from which to measure the rate of energy input or dissipation. We focus on Eq. (1) because it can be determined from external parameters.

Using Eq. (7) as a characteristic velocity scale, we can express the Rhines length as

$$L_\beta = \sqrt{U_\rho/\beta}, \tag{11}$$

and, comparing this to the annulus gap width, construct the parameter

$$L_\beta^* \equiv L_\beta/L, \tag{12}$$

which sets the importance of β in the flow.

We may further define a combination of these two dimensionless numbers as an anisotropy parameter:

$$\gamma \equiv \mathrm{Ro}_T/L_\beta^{*2} = L_\rho^2/L_\beta^2, \tag{13}$$

which appears in earlier analytic work (e.g., Okuno and Masuda 2003; Saito and Ishioka 2013).

Hence, we can construct a new regime diagram that emphasizes the relative importance of the deformation scale, via Ro_T, and the Rhines scale, via L_β^{*2} (Fig. 2). These scales are more readily compared to oceanic values and the result illustrates the progression of laboratory experiments toward the oceanic regime. The experiments in the present work approach dynamic similarity to the ACC more closely than previous experiments, both in terms of the regime Ro_T, $L_\beta^* \ll 1$ and the presence of large-scale forcing.

3. Laboratory apparatus and methods

Experiments were carried out at the Geophysical Fluid Dynamics laboratory at the Australian National University in conjunction with ongoing experiments to observe forcing effects on a channel model ACC (Maher 2010; Merminod 2011). The apparatus used in the current study consists of an annular tank shown schematically in Fig. 3 with dimensions given in Table 1. Details on the construction of the annular tank are given in Hogg and Griffiths (2010). This tank can be rotated at a precise angular velocity ($\pm 1 \times 10^{-4}$ rad s^{-1}) about an axis aligned with the local gravitational field. The working fluid is contained in the annulus between two concentric cylinders at radii a and b and filled to a height h_0 relative to the base of the tank. A clear Plexiglas sheet placed above (but not in contact with) the fluid prevents wind stress from the nonrotating ambient air.

A gradient in the vertically integrated potential vorticity of the fluid,

$$(\zeta + f)/d, \tag{14}$$

is imposed by a gradient in depth provided by radially varying bottom topography (of slope ϕ) and the parabolic free-surface height variation (Fig. 3). This topographic β effect is a common laboratory technique that mimics the gradient in planetary vorticity encountered by geophysical flows (Read 2005).

The free-surface profile in an annulus is a function of rotation Ω and gap dimensions:

$$h(r) = h_0 + \frac{\Omega^2}{2g}\left(r^2 - \frac{b^4 - a^4}{b^2 - a^2}\right), \tag{15}$$

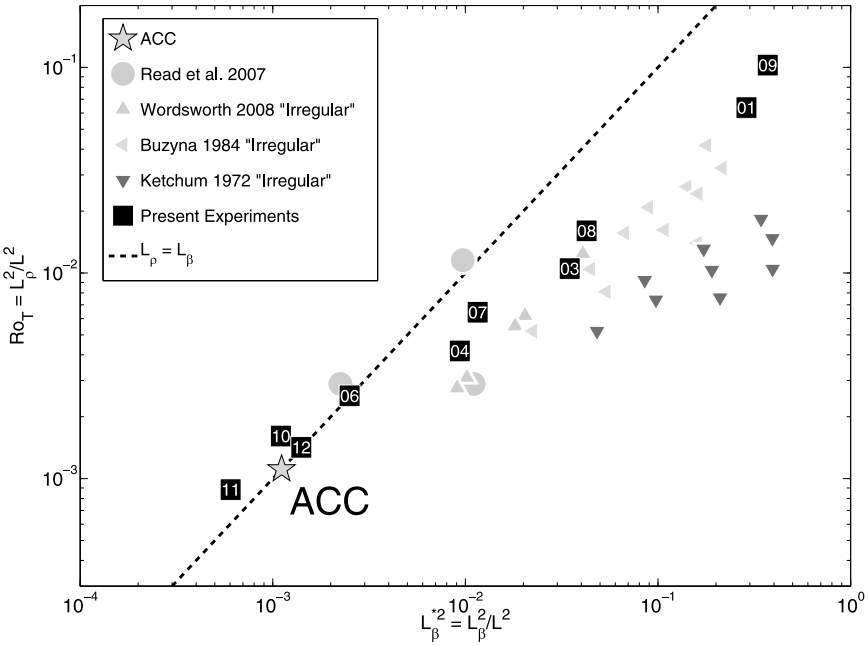

FIG. 2. A comparison between the baroclinic radius of deformation L_ρ and the Rhines length L_β for several annuli experiments. A representative regime for the ACC is calculated from estimates of domain size ($L \sim 1500$ km), deformation radius ($L_\rho \sim 50$ km), and Rhines length ($L_\beta \sim 50$ km). Previous laboratory experiments with a topographic β effect are shown for comparison.

with variables defined in Table 1. The resulting profiles of surface height are shown to scale in Fig. 3b for several representative experimental values. We can then calculate the value for β following Eq. (10) and the nondimensional gradient in slope:

$$s = s_{\text{topo}} + s_{\text{surf}} = \tan(\phi) + \frac{\partial}{\partial r} h(r). \qquad (16)$$

We note that because of the r^2 dependence of h [Eq. (15)], the value for β varies linearly with radius, with a larger value of β at the outer radii where the surface slope is steeper. The value we use in the scaling analysis and report in Table 2 is a bulk value calculated from $s_{\text{surf}} \approx \Delta h/(b-a) = \Omega^2(b+a)/2g$. The maximum relative error associated with this approximation is equal to the nondimensional parameter $(b-a)(b+a)^{-1}$. For the current experiment this is $\approx$0.42, which is comparable to similar experiments in the literature.

It has been noted (Ohlsen and Rhines 1997; Read 2005) that the topographic β effect can only be felt by a density-stratified fluid near the sloping boundaries. However, the efficacy of the topographic β effect as an analog of the true β effect has been borne out in previous laboratory and numerical experiments (Boland et al. 2012; Spall 2013). This is because in practice, the flow is dominated by the gravest baroclinic modes, and these can easily transfer information vertically throughout the water column. LaCasce and Brink (2000) identify a parameter similar to γ [Eq. (13)] that governs the influence of the bottom slope on a baroclinic flow. The present experiments are strongly influenced by bottom slope in their sense (that the value of the parameter be of order unity) and we note that ocean values are near unity as well. The primitive equation simulations of cooling around an island conducted by Spall (2013) bear a striking resemblance to the geometry of the present work and also show spontaneous generation of azimuthal jets. We also point to many previous laboratory experiments demonstrating qualitative analogs to the planetary β effect in baroclinic fluids with sloping topography (e.g., Bastin and Read 1997; Read et al. 2007; Wordsworth et al. 2008).

Thermal forcing in the annulus was achieved by a warm water bath surrounding the outer radius and a cool water bath in the center (Fig. 3). A pair of Julabo FP50-HL refrigerated/heating circulators maintained two-process water lines to within $\pm$0.01°C of a set temperature. A circulation system allowed this water to be exchanged with the inner and outer baths by means of rotating fluid couplings. Some natural heat loss/gain between the circulators and the baths caused the temperatures of the baths to differ from the set points of the

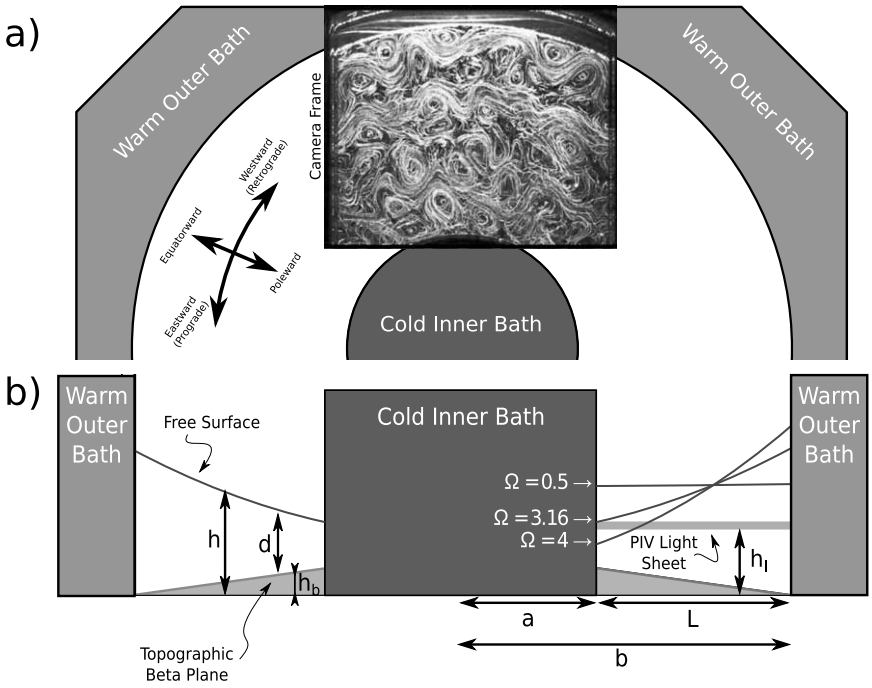

FIG. 3. Schematics of the tank geometry. (a) Plan view showing the annular domain, the cylindrical polar coordinate system $\hat{\theta}$, $\hat{r}$, and the field of view (FOV) of the imaging camera. (b) Vertical cross section shows (to scale) the dimensions of the inner and outer radii (a and b), the gap width L, the depth of the fluid layer d, the height of the free-surface h, and the height of the sloping bottom topography h_b. The horizontal light sheet that illuminates the particles is shown on the right at height h_l. For different rotation rates, the parabolic free surface obtains different height profiles. Several of these are shown to scale for representative rotation rates [Ω (rad s^{-1})]. Note that for $\Omega \sim 4$ rad s^{-1}, the light sheet intersects the free surface.

circulators. This rate of heat loss was a constant, amounting to a temperature offset that appeared to vary only with the experimental regime. Lower-resolution ($\pm$0.1°C) temperature probes in the inner and outer baths were used to compensate empirically for this offset and measure the imposed ΔT for each experiment. The variance of the bath temperatures with time is an order of magnitude smaller than the reported accuracy of the imposed ΔT for each experiment.

Before data collection, the apparatus was allowed to spin up from rest over a period of $\approx$15 h. An adjustment time of $\approx$1 h was allowed between each iterative change in forcing parameters. Data were then taken for 1 h (with the exception of experiment GT10, which was run for 0.5 h).

Visualization of the flow was made with neutrally buoyant particles illuminated by a horizontal light sheet at middepth within the fluid (Fig. 3). Pliolite particles

TABLE 1. Experimental parameters.

Symbol	Description	Value	Uncertainty
a	Inner cylinder radius (mm)	200	$\pm$0.1
b	Outer cylinder radius (mm)	487.5	$\pm$0.1
L	Annulus gap width (mm)	287.5	$\pm$0.1
$h_b(r)$	Height of the bottom topography (mm)	0–37	$\pm$0.1
ϕ	Slope of the bottom topography (°)	7.4	$\pm$0.2
h_l	Height of the PIV light sheet (mm)	95	$\pm$5
h_0	Mean (fill) height of the free surface (mm)	150	$\pm$1
d	Mean depth (mm)	120	$\pm$1
Ω	Apparatus rotation rate (rad s^{-1})	0.5012–4.0000	$\pm 1 \times 10^{-4}$
ΔT	Temperature gradient across annulus gap (°C)	11.0–19.9	$\pm$0.1

TABLE 2. List of experiments.

Expt ID	Ω ($\pm 10^{-3}$ rad s^{-1})	ΔT (± 0.1 K)	s	Ta ($\times 10^{11}$)	E ($\times 10^{-4}$)	Ro_T	L_β^* ($\times 10^{-3}$)	L_ρ (mm)	L_β (mm)	$L_{\beta,\mathrm{rms}}$ (mm)
GT09	0.501	20.0	0.143	0.152	0.386	0.389	372	87.3	176	69.6
GT01	0.501	15.5	0.143	0.152	0.386	0.301	288	76.9	155	—
GT08	1.258	19.7	0.2675	0.9596	0.154	0.0607	42.6	34.5	59.4	33.1
GT03	1.258	16.1	0.2675	0.9596	0.154	0.0496	34.8	31.2	53.7	—
GT07	1.994	19.9	0.4906	2.411	0.0970	0.0244	11.6	21.9	31.0	21.1
GT04	1.995	16.1	0.491	2.413	0.0969	0.0197	9.36	19.7	27.8	—
GT06	3.161	19.6	1.051	6.059	0.0612	0.0096	2.50	13.7	14.4	—
GT05	3.163	16.1	1.053	6.066	0.0611	0.0079	2.05	12.4	13.0	—
GT10	4.000	20.0	1.611	9.702	0.0483	0.0061	1.10	10.9	9.56	7.22
GT12	3.161	11.0	1.051	6.059	0.0612	0.0054	1.41	10.3	10.8	8.10
GT11	4.003	11.0	1.61	9.716	0.0483	0.0033	0.604	8.10	7.08	11.1

($\rho = 1.033\,\mathrm{g\,cm^{-3}}$) were graded by diameter to 125–250 μm using a standard set of sieves and coated with a wetting agent (detergent) to prevent conglomeration. The light sheet was produced by a slide projector aimed through a rectangular mask affixed to the outside of the outer Plexiglas tank, which was constructed with clear, flat faces (shown in Fig. 3) to prevent optical distortion. The slide projectors were placed on the rotating table high above the tank. Front surface mirrors were used to direct the light, resulting in a pathlength of >2 m and a near-parallel light sheet. The working fluid consisted of a de-aired salt solution whose density was adjusted to match that of the Pliolite particles to within $\Delta\rho/\rho \approx 10^{-3}$, ensuring that they would be neutrally buoyant throughout the experiment. Even though the buoyancy of the working fluid varied somewhat (due to the spatial variation in temperature), some natural variation in the particles' density ensured the flow was seeded throughout the domain. The inner and outer walls of the warm bath were made of Plexiglas to allow light to pass into the interior. A horizontal plane of width ~1 cm was illuminated at a constant depth of h_l using a slide projector aimed through a slitted mask affixed to the outer wall of the tank, which was flat to prevent optical distortion. The motion of the particles within the illuminated sheet was recorded from above the annulus using digital video camcorders mounted high on the rotating platform. The video was parsed into still images (3 frames s^{-1}) using the time-lapse frame-grabbing features of BTVpro software. Eulerian vector fields were then derived through particle image velocimetry (PIV; Adrian 2005) at 3 Hz using MATLAB and the PIVlab toolkit (Thielicke 2014; Thielicke and Stamhuis 2010). The images, whose field of view spanned the gap width (as seen in Fig. 3a), had a resolution of 720 × 576 pixels (px). Interrogation windows of size 15 px yielded a 35 × 41 grid of Eulerian time series with an ≈8-mm spacing.

A very slight shaking of the cameras with the rotation of the table induced an apparent motion of the particles between frames, resulting in spurious velocities in the derived Eulerian vector fields. However, because the (largely geostrophic) flows being considered evolve on a much slower time scale than the rotation period, a low-pass Butterworth filter with a cutoff at 0.08 Hz (the inertial frequency of the most slowly rotating experiment) was sufficient to remove the camera shaking, while not filtering out the essential evolution of the flow. Direct comparisons between the raw particle images and the filtered velocity fields confirmed that only spurious motions were removed.

For some experiments (shown in Fig. 4), 2D temperature fields oriented in the $(\hat{r}, \hat{z})$ plane were obtained by means of a set of six traversing thermistor probes. The thermistors were held by a computer-controlled armature that could be moved vertically through the working fluid at a speed of ≈20 mm s^{-1}. Six simultaneous thermistor profiles were taken, located between 219- and 469-mm radii and spaced 50 mm apart (grid lines in Fig. 4). The resulting data were parsed into 1-mm vertical bins and registered to a 2D grid.

4. Results and discussion

a. Qualitative description

Streak photos of the flow (Figs. 5, 6), made by combining consecutive raw images of neutrally buoyant particles, show the flow is predominately in the eastward (prograde) direction, as predicted from the first-order thermal wind balance. As rotation increases (at a constant ΔT), the eddy length scales decrease, broadly consistent with the decreasing baroclinic radius of deformation (Table 3). At the same time, the slope of the free surface becomes steeper, causing the strength of β to increase and the Rhines scale L_β to decrease. Time-mean Eulerian fields (Fig. 7) show a distinct banded structure for the experiments with higher Ω and lower ΔT.

Starting with the least turbulent experiments (Table 3 and the top left corner of Fig. 6) and working toward

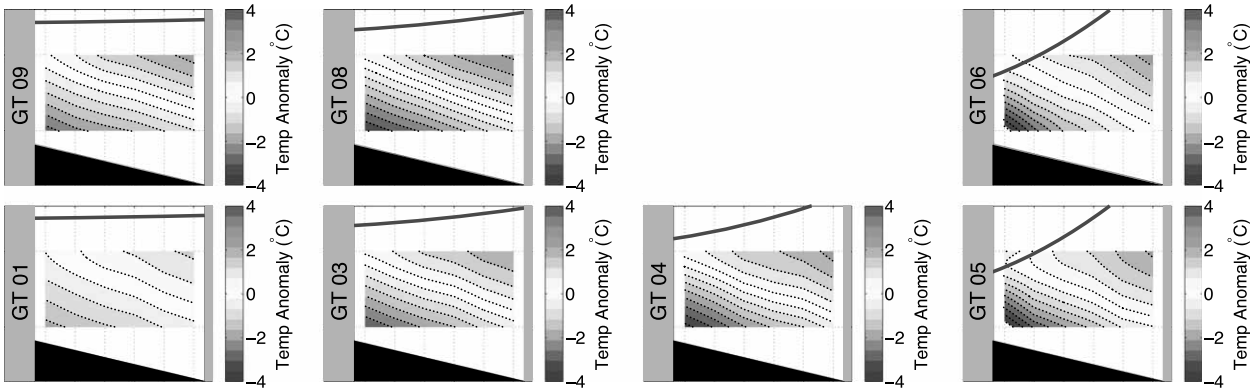

FIG. 4. Time-averaged (r, z) temperature fields measured by a set of six traversing thermistors averaged over the duration of each experiment and referenced to the average measured temperature. The experiments are arranged by increasing the rotation rate from left to right and imposed ΔT from top to bottom (Table 2). The meridional locations of the six thermistor profiles are shown by the dotted vertical lines (the grid has been stretched vertically to show detail). The temperature fields are shown relative to the bounding surfaces: the hot and cold walls (gray), the topographic β plane (black), and the fluid free surface (blue line).

smaller ΔT and larger Ω, we identify four-jet regimes. Using nondimensional wavenumber notation, these are $k_{\text{jet}} \approx 1$, a single, irregular, prograde jet (GT09, GT01, GT08, and GT03); $k_{\text{jet}} \approx 2$, one retrograde and two prograde jets (GT07 and GT04); $k_{\text{jet}} \approx 3$–4, two prograde jets near the walls and eddy-forced prograde jets in the central radii (GT06, GT05, and GT10); and $k_{\text{jet}} \approx$ 4–5 that has a larger number of weaker jets (GT10 and GT11). Wavenumber spectra (Fig. 8) support this description of the progression of jet regimes.

Experiments GT09 and GT08 ($k_{\text{jet}} \approx 1$) are each dominated by a single, prograde jet. Eddies of approximately ⅓ to ½ the annulus gap width are spawned from the hot and cold walls and cause long time-scale meanders of the main jet with no obvious periodicity. Because of this intermittent ''switching'' behavior in the motion, this has been termed irregular flow or geostrophic turbulence (Buzyna et al. 1984; Ketchum 1972). Experiments GT09 and GT08 have the lowest value for β and so bear the most resemblance to the regimes identified by classical annulus studies, although it is difficult to ascertain the exact effect of the small β that is present without a proper control experiment.

Between $\Omega \approx 1.3$ and $2\,\text{rad}\,\text{s}^{-1}$, the main prograde jet has split, and in experiments GT07 and GT04, the flow is dominated by two prograde jets, each hugging a bounding wall with a single, retrograde jet between them ($k_{\text{jet}} \approx 2$).

At higher Ta, β, and lower Ro_T (GT06), the wall jets are confined more closely to the boundaries, and two new prograde jets appear in between them. GT12 has a similar value for β and Ta as GT06, but a lower Ro_T. Consequently, it has very low velocities, which make resolving fine features difficult. While its jets are weaker than GT06, upon averaging in time, GT12 seems to have a similar number of jets.

Further experiments were carried out at even higher values of Ω (GT10 and GT11). Because of the extreme deformation of the free surface (Fig. 3b), the light sheet was not entirely immersed in the fluid, and a full meridional transect of velocities could not be taken. However, the streak images show qualitatively that the progression to higher numbers of jets seems to continue with the movement to more turbulent regimes.

b. Eddy zonal-mean interaction

As the system moves into the turbulent regime, baroclinic instability produces eddy fluxes that, in zonal

FIG. 5. Long exposure image of neutrally buoyant particles in experiment GT06. The flow is predominantly in the prograde direction [counterclockwise (CCW), to the left in this plot]. The exposure is ≈13 s. (Animated version in supplementary material.)

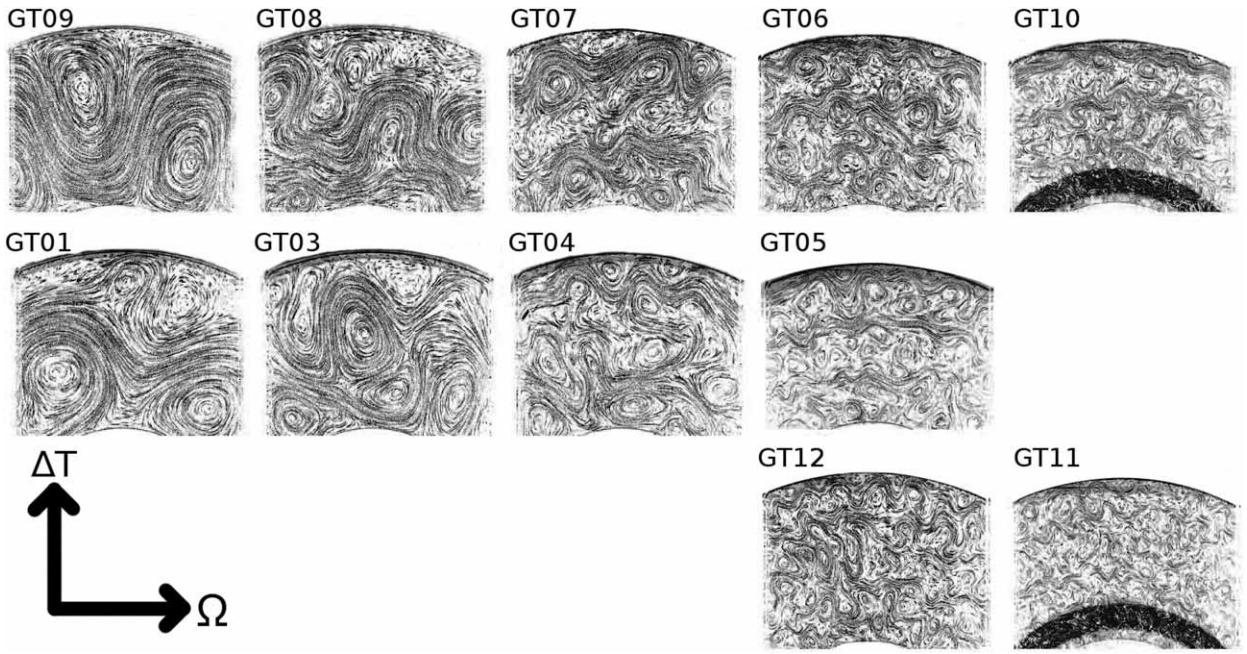

FIG. 6. Streak images of different regimes. The experiments are arranged from left to right in order of increasing rotation rate Ω and from top to bottom in order of decreasing ΔT (mirroring the placement of the black boxes in Fig. 1). At high rotation rates (GT10 and GT11), the light sheet penetrated the free surface, causing the overexposed band near the inner wall. (Animated version in supplementary material.)

average, redistribute the momentum to drive the jets (Vallis 2006).

The velocity fields can be separated into zonally averaged and residual components

$$\mathbf{u} = \langle \mathbf{u} \rangle + \tilde{\mathbf{u}} \tag{17}$$

and into time-averaged and perturbation components

$$\mathbf{u} = \overline{\mathbf{u}} + \mathbf{u}'. \tag{18}$$

Using Eq. (17), we can construct the zonally averaged zonal momentum equation, and, following Read et al. (2007) and references therein, the dominant balance is the acceleration of the mean flow by eddies and the scalar Reynolds flux divergence:

$$\frac{\partial \langle u_\theta \rangle}{\partial t} \sim \frac{1}{r} \frac{\partial}{\partial r} [r(\tilde{u}_\theta \tilde{v}_r)] \tag{19}$$

[see also terms 1 and 5 of Eq. (7) in Read et al. (2007)]. The time mean of the quantity on the right of Eq. (19) is displayed alongside the zonal velocity $\overline{\langle u_\theta \rangle}$ in Fig. 9.

Starting with the two cases of GT04 and GT07, we find a divergence of eddy momentum centered on the retrograde jet (dotted line) and a convergence centered on the prograde jets (dashed lines). This pattern is also present in the freely evolving midlatitude jet present in GT06. However in this latter case, the divergent regions bordering the prograde jets are weaker in magnitude. Consequently, there is less eddy driving of the retrograde jets, which are correspondingly much weaker than in the GT07 case. Here, the retrograde jets are only visible as local reductions in the mean zonal flow and do not result in negative Eulerian velocities. This momentum flux profile is consistent with the eddy driving mechanism for the numerical experiments of Panetta (1993).

Even with the decreased velocities of GT12, a pattern of eddy flux convergence consistent with the previous experiments is still visible. The slight misalignment with the jet locations is likely due to an increased unsteadiness of the jets in this regime.

c. Scaling revisited

An assumption in our earlier scaling arguments is the use of the bulk thermal wind shear U_ρ as representative of an rms zonal velocity scale. The relationship

TABLE 3. Nondimensional parameters compared between the Southern Ocean and the laboratory.

	Parameter	Southern Ocean	Laboratory
δ	Aspect ratio	10^{-3}	0.5
Ro	Rossby number	10^{-4} to 10^{-3}	10^{-3} to 0.5
Ta	Taylor number	10^{24} to 10^{26}	10^{9} to 10^{11}
E	Ekman number	10^{-7}	10^{-6} to 10^{-5}
L_β^2/L^2	Scaled Rhines length	10^{-3}	10^{-4} to 10^{-2}

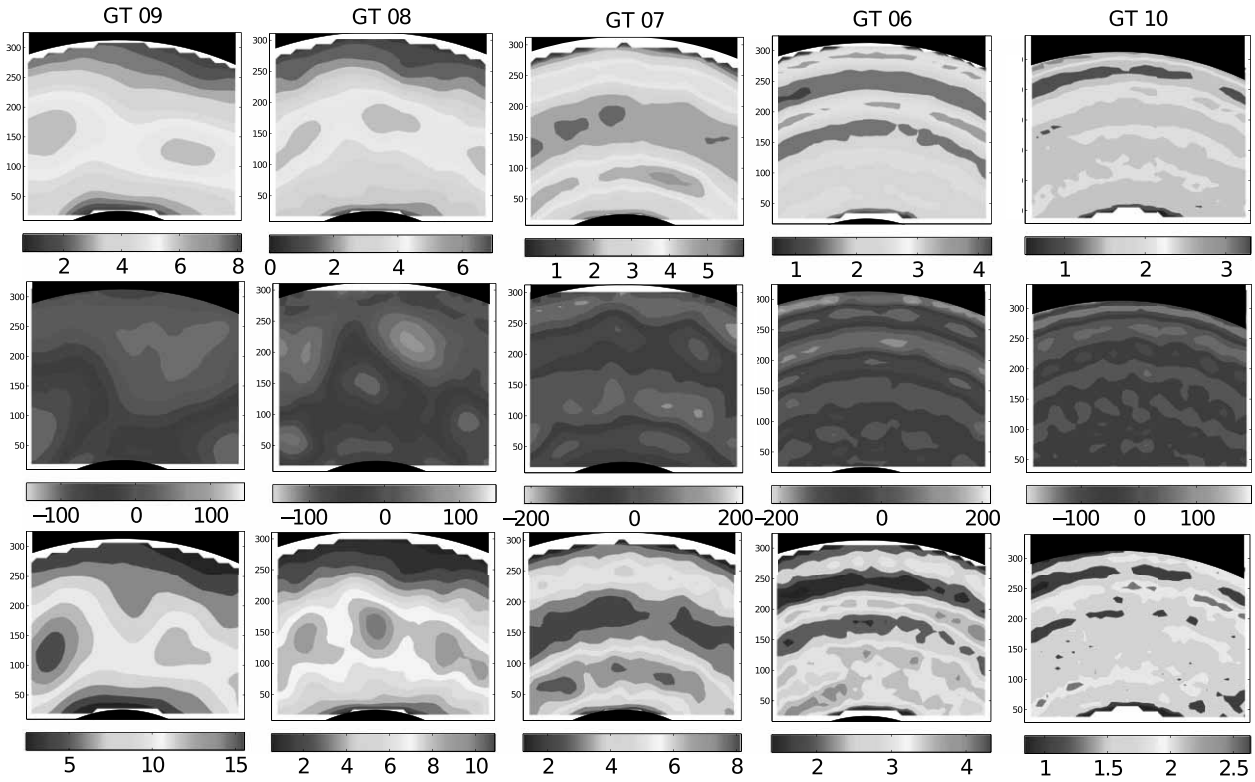

FIG. 7. Time-averaged fields derived from PIV data plotted for several experiments. (top to bottom) Speed (mm s^{-1}), vorticity (s^{-1}), and eddy kinetic energy ($mm^2 s^{-2}$). The experiments are ordered (left to right) by decreasing Ro_T and L_β^*. Even with the considerable meandering visible in the streak animations, one can see the two-jet structure in GT07 and the 3–4-jet structure in GT06.

between the bulk thermal wind and the measured flow from particle image velocimetry (PIV) analysis is shown in Fig. 10. The two velocity scales approach one another at high rotation rates, that is, in the multiple jet regime.

The divergence at lower rotation (and higher velocities) is likely due to a sampling issue associated with the horizontal velocities being recorded at depth instead of at the surface. The height of the horizontal plane of illuminated particles does not change from experiment to experiment, while the radial distribution of water depth does change. Velocities measured in the bulk of the fluid are smaller in magnitude compared with the surface. Hence, as Ω decreases, the light sheet is deeper over much of the radius and velocities in the light plane are smaller.

As a practical matter, because our bulk Rhines parameter k_β is also based on the external parameter U_ρ, we define the internal Rhines scale

$$L_{\beta,\mathrm{rms}} \equiv \sqrt{U_{\mathrm{rms}}/\beta}, \tag{20}$$

based on the total rms velocity.

A jet spacing, defined as the distance between maxima of the zonally averaged flow, shrinks in proportion to the decreasing bulk Rhines scale (Fig. 11a) based on the externally imposed thermal wind. The relation to jet spacing is in either case very similar (Figs. 11a,b), as would be expected. Read et al. (2007) report a jet spacing (their case III, similar to GT06) that falls close to the same relationship (Fig. 11b).

d. Spectral characteristics

The two-dimensional eddy kinetic energy spectra S is

$$\overline{S(k_x,k_y)} = \frac{1}{2}\overline{\left|\widehat{u'}^2 + \widehat{v'}^2\right|}, \tag{21}$$

where the overline represents an average in time, the hat represents the Fourier transform, and the u' and v' perturbation velocities [Eq. (18)] were computed from the Cartesian velocity data on a 262 × 229 mm square subdomain centered around $\theta = \pi/2$. A Cartesian coordinate system was used since the domain is a small sector of the full annulus and the curvature of the bounding walls is considerably smaller than that of the eddies. The influence of this choice is minimal.

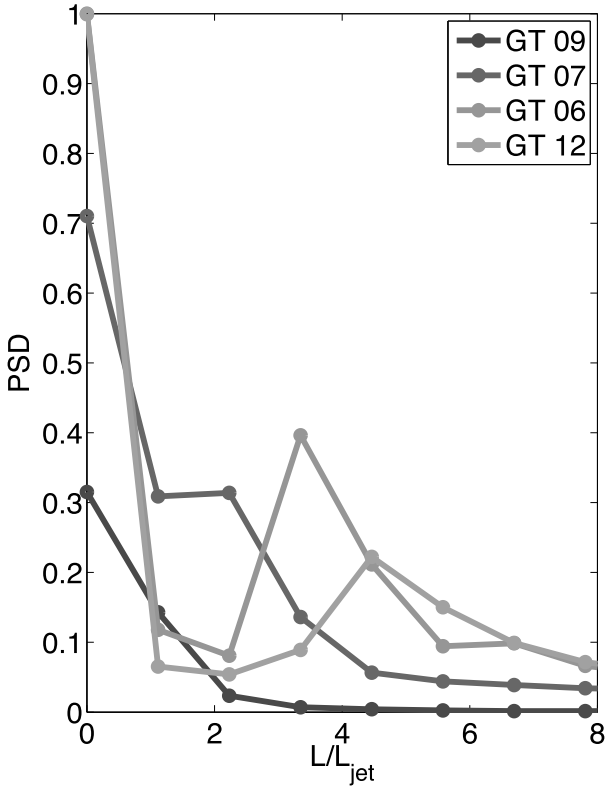

FIG. 8. Meridional FFT of time-averaged zonal velocity for several experiments. Note how the peak in meridional wavenumber (i.e., number of jets) increases from GT09, to GT07, to GT06, to GT12.

Following Vallis and Maltrud [1993, their Eq. (2.11)], we plot the transition wavenumbers:

$$k_x^R = \sqrt{\beta/U_{\rm rms}}\cos^{3/2}\varphi, \tag{22a}$$

$$k_y^R = \sqrt{\beta/U_{\rm rms}}\cos^{1/2}\varphi\sin\varphi, \tag{22b}$$

where $\varphi = \arctan(k_y/k_x)$ together with energy (Fig. 12). The transition represents a rough boundary between smaller-scale turbulence and larger-scale Rossby wave dynamics. As expected, the experiments where the β effect is significant (i.e., $L_\beta^* \ll 1$; GT07, GT10, and GT12) have energy troughs and peaks that roughly correspond to the size and shape of this boundary creating a picture similar to the ''dumbbell'' plots of Vallis and Maltrud (1993). In contrast, the lower Ω experiments (GT09 and GT08) have a scale for L_β that is comparable to the gap width, and the 2D spectra are more isotropic.

The classical picture of the energy cascade in geostrophic turbulence (see, e.g., Salmon 1978, 1980; Vallis and Maltrud 1993) envisions four or more distinct

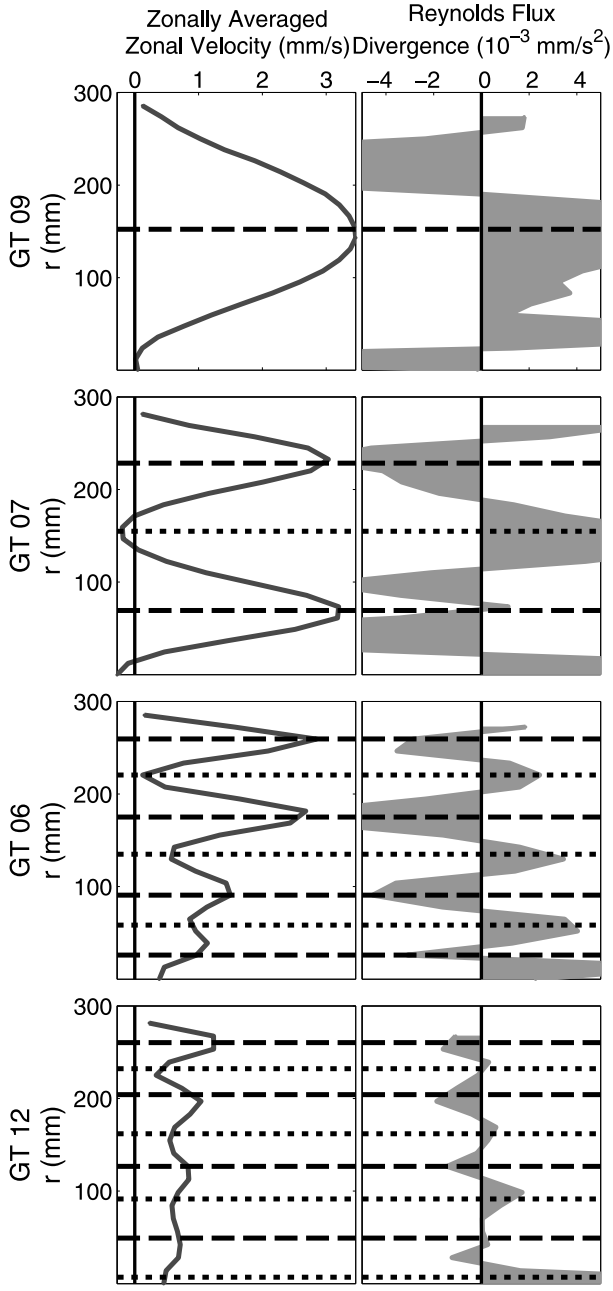

FIG. 9. Relationship between zonal mean and eddy components. Temporally and zonally averaged zonal velocity $\langle\overline{u_\theta}\rangle$ and Reynolds flux divergence $\overline{(1/r)\partial(r\langle u_\theta' u_r'\rangle)/\partial r}$ for several experiments ordered by (top to bottom) decreasing Ro_T and increasing β. To facilitate comparison, a dashed line is placed at a radius corresponding to every prograde (eastward) jet, and a dotted line is placed corresponding to every retrograde (westward) jet.

spectral ranges partitioned by the Rhines wavenumber k_β, dissipation at the high and low ends of the spectrum, and some energy injection scale. This latter scale is sometimes identified with the deformation radius, but in real flows this is not a simple source localized in

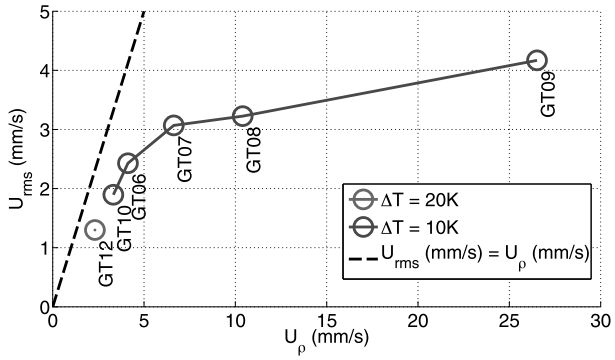

FIG. 10. Relationship between $U_{\rm rms}$ and U_ρ.

wavenumber. Barotropic energy participates in a forward cascade for $k > k_\rho$ and an inverse cascade for $k < k_\rho$. This picture is apparently consistent with slopes from numerical (e.g., Vallis and Maltrud 1993) simulations, atmospheric observations (Gage and Nastrom 1986), and laboratory (e.g., Afanasyev and Craig 2013) experiments.

To assess the applicability of the classic scaling arguments cited above, representative spectra are plotted in Fig. 13. If we explicitly remove the zonal average from each dataset and produce spectra of the residual $\tilde{\mathbf{u}}$, the results are essentially the same. All spectra show a peak at lower wavenumbers, which migrates to higher wavenumber following closely an increasing k_β at greater rotation rates. Dissipation in Ekman and sidewall layers at the lowest wavenumbers and by direct viscous effects at the highest wavenumbers lower the energy levels at either end of the spectrum. Although the experimental regimes are not dependent on viscous effects (e.g., as indicated by Fig. 1), the highest resolved wavenumber displayed (after averaging) represents a scale just under 1 cm (with Reynolds number $\gtrsim 10^2$) and approaches the range influenced by viscous diffusion.

In cases GT08 and GT09 (lower rotation and smaller k_ρ), the spectral slopes at wavenumber greater than k_ρ follow roughly a $-5/3$ slope (Fig. 13). At the high-wavenumber end of the spectrum, the effective Rossby number is large, consistent with internal wave–related turbulence. Some evidence exists for a $-5/3$ spectrum in ocean observations, at lower (relative to internal wave scales) wavenumbers (Klymak and Moum 2007; Holbrook 2005). This may be consistent with atmospheric observations (Gage and Nastrom 1986), although the slopes are not expected to be identical.

The spectra of experiments with jets (GT06 and GT12) are dominated by steeper slopes, rising to greater than -4 in the strong β cases. Read et al. (2007) observe a -5 slope, but only in the zonally averaged spectra of their case III (which was most similar in regime to our GT06). Numerical experiments by Chekhlov et al. (1996), Huang et al. (2001), and Galperin et al. (2006, 2010) suggest a -5 slope in the zonally averaged ($\langle \mathbf{u} \rangle$) spectra. A similarly steep spectrum appears in flows of a zonal jet regime in the North Pacific Ocean (Galperin et al. 2004). To some extent this is an expected feature of multiple zonal jet flows and has been found to be a robust quality of numerical experiments of turbulence on a sphere or β plane. A -5 slope (Rhines 1975) may result from the retention of energy at larger scales due to an ongoing process of jet mergers and representing an ‘‘equilibrium

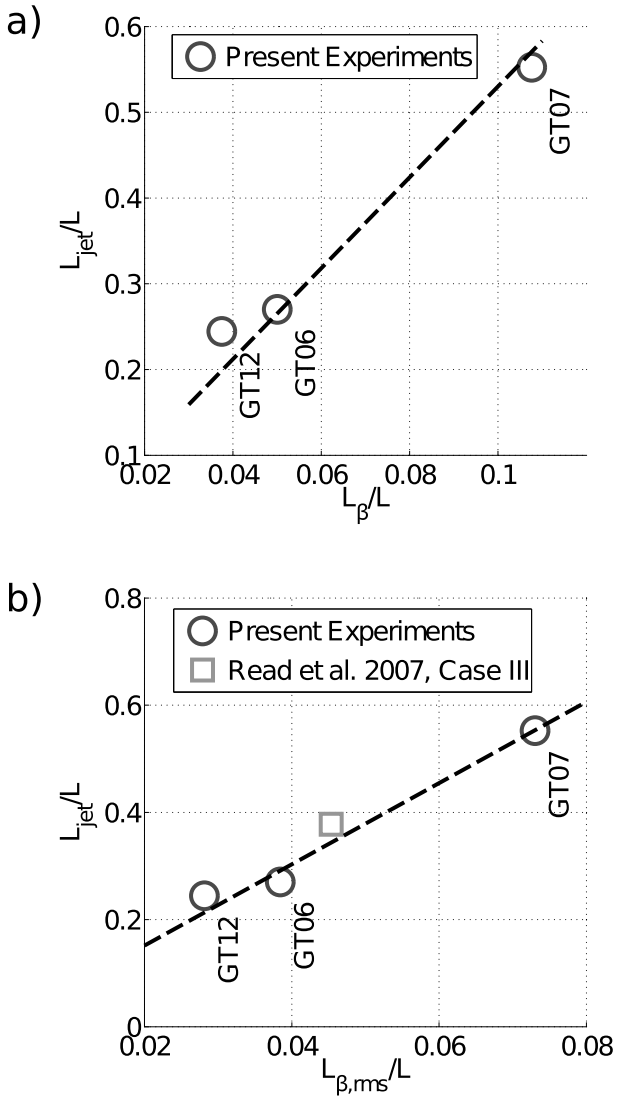

FIG. 11. Jet spacing $L_{\rm jet}/L$ scaled by gap width L vs a Rhines parameter calculated from the (a) external U_ρ scaling and (b) one based on the measured rms velocity $U_{\rm rms}$. The jet spacing is determined from the average distance between local prograde maxima of the zonally averaged zonal flow, depicted in Fig. 9 (circles). In (a) $L_{\rm jet} \sim 5L_\beta$ and in (b) $L_{\rm jet} \sim 8L_{\beta,\rm rms}$ (dashed lines). For comparison, we plot case III from Read et al. (2007) using a jet spacing derived from their Fig. 14 (square).

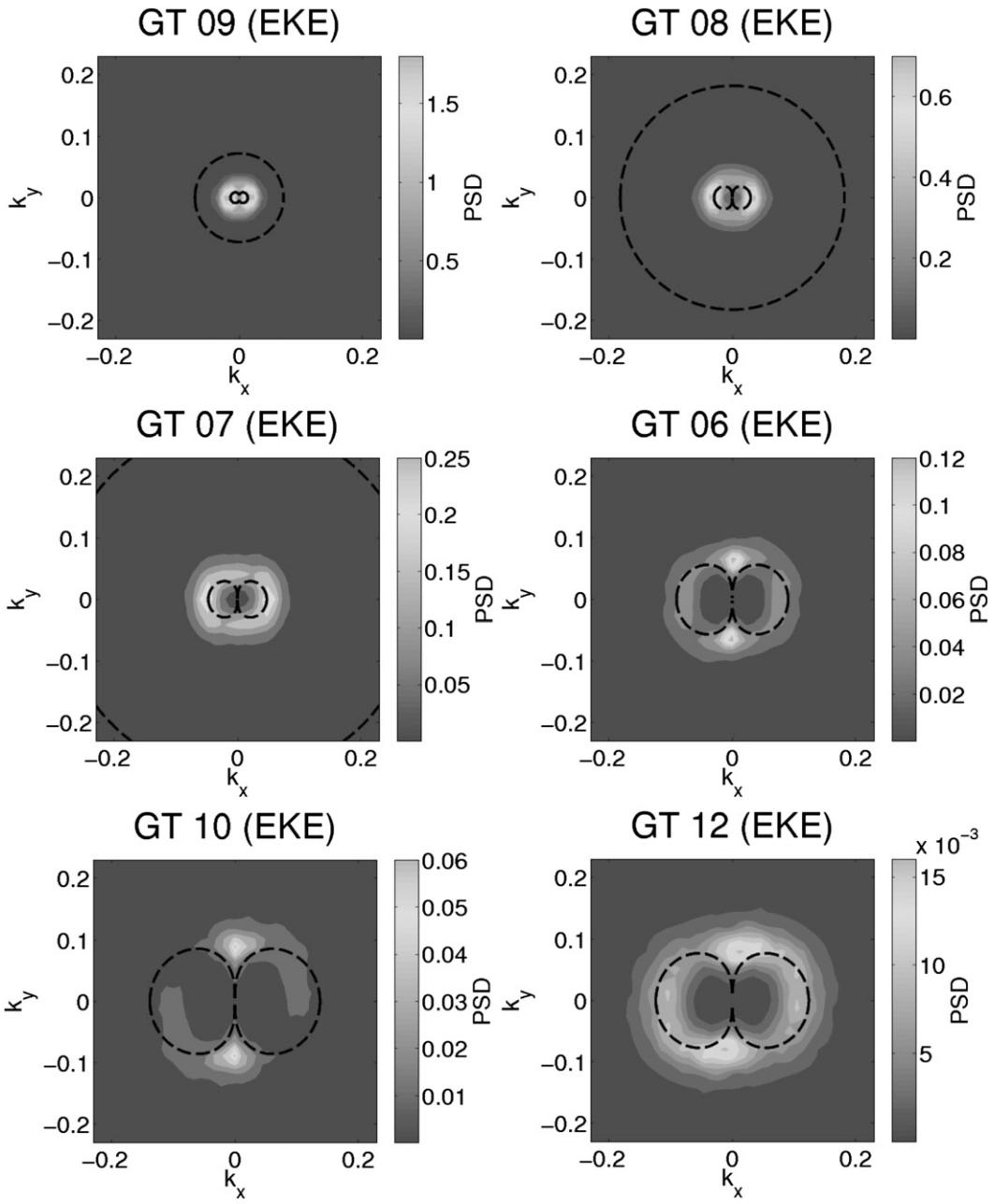

FIG. 12. Zonal and meridional wavenumber spectra of Cartesian EKE fields shown relative to the Rhines transition wavenumbers [Eq. (22)] and the magnitude of k_ρ (dashed circle). The 2D spectra were computed from a 262 × 229 mm square subdomain and averaged over the duration of the experiment. The contours are of power spectral density (PSD), and the axes are Cartesian wavenumber space (rad mm^{-1}).

spectrum'' for energy exchange (Huang et al. 2001; Sukoriansky et al. 2002).

There are several caveats that should be noted. Because of the relatively high rotation rates of these experiments and significant free-surface deviation, velocities derived from a horizontal slice through the fluid are not made at a constant depth. Since velocities can vary significantly with depth in the baroclinic annulus (Lappa 2012), it is possible some bias has been introduced into the spectra due to sampling. Similar effects would have been present for the experiments of Read et al. (2007) and Zhang and Afanasyev (2014), without apparent bias. Suitably long particle tracks (Fig. 5) also imply that flow normal to the light sheet was

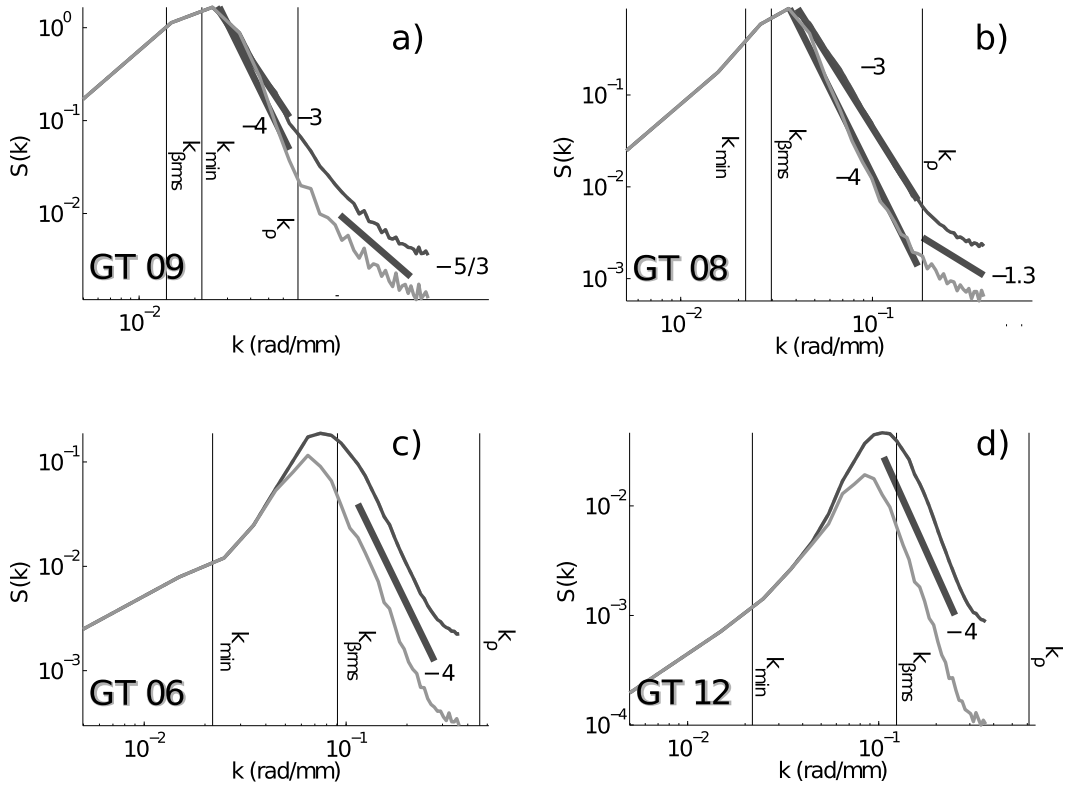

FIG. 13. Spectral slopes of eddy kinetic energy. Also displayed are the annulus gap wavenumber $k_{\min} = 2\pi/L$, deformation scale $k_\rho = 2\pi/L_\rho$, and Rhines wavelength ($k_{\beta,\mathrm{rms}} = \sqrt{\beta/U_{\mathrm{rms}}}$). Curves display the 2D spectrum at a particular $|\mathbf{k}|$ regardless of direction (blue line) and the spectrum of long zonal scales (red; $k_x < 2k_{\min}$).

not a source of contamination. An additional point is that the β effect is not constant with the radius. Any effect this might have on the isotropic spectrum is unclear, however, as this effect, if significant, would more likely preferentially affect the very long zonal wavelengths not resolved in our domain of measurement.

e. *Time-varying structure*

The complex interplay of transient and time-mean features is one of the most interesting aspects of multiple zonal jets, and a major advantage of a laboratory experiment is the ability to observe these at high spatial resolution and for long periods of time.

Hovmöller (r, t) plots of the zonally averaged zonal flow (top panels of Fig. 14) illustrate the time-varying character of the flow. The zonal average is taken to highlight the motion of the jets themselves, rather than coherent eddies propagating through the field of view. In parallel with these plots, spectrograms depict the instantaneous dominant meridional wavenumber (plotted in parallel with the Hovmöller time series in Fig. 14).

For the single jet experiments (GT09 and GT08), the location of the single jet drifts throughout the domain with no obvious periodicity, consistent with irregular structural vacillation reported in previous annulus experiments conducted in a similar regime (Buzyna et al. 1984; Ketchum 1972). In the case with two jets (GT07), the jet cores do not drift considerably, and there is very little change in the meridional structure with time, although brief periods of apparent jet interaction can be observed.

In the cases with multiple zonal jets (GT06 and GT12), the time-varying structure becomes more complicated. Here, one sees transient propagation events (denoted by dashed black lines) where the pattern of alternating jets remains coherent and of constant wavenumber while the jet cores drift meridionally (such as events c, d, and e of GT06). Similar events were observed by Panetta (1993, p. 2094) purportedly as a natural consequence of the domain size being a noninteger multiple of the preferred jet width.

A related observation is that the obvious alternating jet structure with a clear meridional Fourier peak is only present for intermittent periods, punctuated by the transient propagation events. In some cases, one can see that these events can result in the transition between dominant wavenumbers of flow (see, e.g., the transition between wavenumber 5 and 4 in experiment GT12 at ≈400 s). These transients always originate on the cold

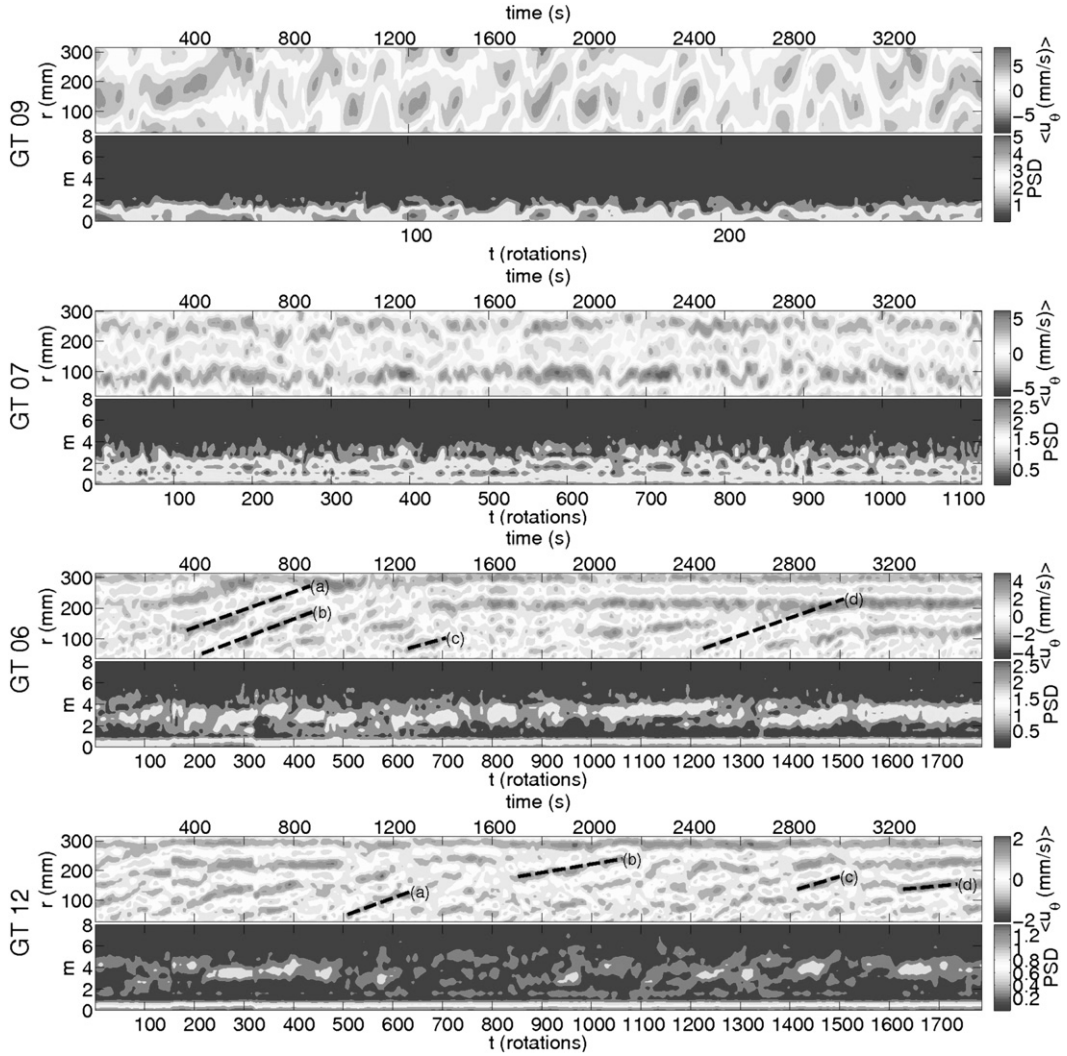

FIG. 14. Time-varying structure for several representative experiments. Top of each panel displays r vs t Hovmöller plots of Eulerian zonal velocity (mm s^{-1}) zonally averaged over a zonal domain of ≈200 mm. Bottom of each panel displays spectrograms showing the change in the structure of the meridional FFT with time (time on the abscissa, meridional wavenumber on the ordinate). For experiments GT06 and GT12, characteristics corresponding to propagation events are highlighted with dashed lines. The letters reference the propagation velocities of these events detailed in Table 4.

(polar) side and propagate to the warm side (equatorward). Table 4 summarizes the propagation speeds highlighted in Fig. 14. The experiments were spun up from rest over a period of ≥10 h, about 1 h was allowed after each iterative change in forcing parameters. This time is much longer than the transit time across the domain; however, it is possible that these transient events are associated with a long-term thermal equilibration.

5. Conclusions

Early work with the thermally driven annulus described the transition from stable symmetric overturning states to wave regimes and finally a transition to a geostrophic turbulent flow. More recent laboratory studies have investigated the emergence of multiple jets in much higher Ta regimes of turbulent flow. To compare better the Read et al. (2007) Grenoble experiment to our experiment, we can construct a salt stratification analog to Ro_T. Their apparatus had access to regimes of considerably higher Ta and lower E (approximately two orders of magnitude; Fig. 1), mainly because the apparatus size is so large. However, when the strength of their β effect is nondimensionalized, we find that it is on the same order as the present experiments (Fig. 2).

TABLE 4. Propagation speeds of transient events. Letters refer to characteristics marked in Fig. 14. The velocities are scaled by $\beta L_{\beta,\mathrm{rms}}^2$.

GT06 event	Speed ($\mathrm{mm\,s^{-1}}$)	Scaled speed	GT12 event	Speed ($\mathrm{mm\,s^{-1}}$)	Scaled speed
a	0.2915	0.120	a	0.3046	0.234
b	0.3063	0.126	b	0.1422	0.109
c	0.2242	0.092	c	0.2500	0.192
d	0.2865	0.118	d	0.0783	0.060

Furthermore, we note that the number of jets within the gap width in their experiments (they report three to four prograde jets in their case III) is comparable to ours. This supports the idea that the formation of multiple jets shows a lack of dependence on Taylor number for $\mathrm{Ta} \gtrsim 10^8$.

A simple scaling based on the thermal Rossby number on the one hand, and the Rhines scale on the other, suggests that the laboratory setting with large-scale forcing is approaching a multiple jet regime similar to the ocean. The zonal and meridional wavenumber spectra show the characteristic dumbbell shape of anisotropic motion (Vallis and Maltrud 1993). Here, this character is seen to be associated with the development of multiple jets with forcing at the largest scales.

The spectral slopes observed in turbulence can be indicative of the dominance of different physical processes (Callies and Ferrari 2013). In the most energetic parts of the ocean (such as the ACC), KE spectra are found to be much steeper than the -3 slope predicted from rotating turbulence alone (Xu and Fu 2011). While some work predicts a -5 spectrum for the zonally averaged field, and a shallower spectrum for the residual field, our zonal spectra are broadly consistent for both total and residual. This result is robust to different methods of calculating the residual spectra.

The extent to which our laboratory experiment actually represents the ocean is not yet clear. Wind-driven forcing and topography has been neglected in the present study, which raises questions concerning the role of dissipation, for instance, of topographic form stress compared to Ekman layer dissipation. Nevertheless, we do attain geostrophic turbulence in a strong β regime driven by large-scale baroclinic instability. In the strongly turbulent cases, spectral slopes steepen, consistent with turbulence theory.

The notion of the merging and splitting of jets is another key aspect of the oceanic regime and the ACC in particular. While this clearly involves the ridges, gaps, and other nonuniform topography in the ocean, we infer that substantial jet interaction appears away from such features too. In the experiments, jet interaction occurs intermittently, suggesting an ongoing dynamical adjustment throughout the evolution of the system at low Ro_T and low L_β^*, with meridional propagation and transitions between jet number being key elements of regime behavior.

Acknowledgments. We thank Andy Hogg for his helpful comments and support in hosting CAS, Dhruv Balwada, and two anonymous reviewers who greatly improved this paper. The laboratory portion of this work was performed using the facilities of the Geophysical Fluid Dynamics Laboratory at the Australian National University. The experiments would not have been possible without Anthony Beasley and Ben Tranter who were responsible for the construction and modification of the apparatus, as well as producing and troubleshooting the traversing thermistors. Nicola Maher and Simon Merminod were also essential in the development of the experimental techniques and data analysis methods for the apparatus. We thank them for sharing their technical skills and help. This work was supported by NSF 0927583, NSF 0622670, and NSF 1231803, as well as ARC DP120102744.

REFERENCES

Adrian, R. J., 2005: Twenty years of particle image velocimetry. *Exp. Fluids,* **39,** 159–169.

Afanasyev, Y. D., and J. Wells, 2005: Quasi-two-dimensional turbulence on the polar beta-plane: Laboratory experiments. *Geophys. Astrophys. Fluid Dyn.,* **99,** 1–17, doi:10.1080/03091920412331319513.

——, and J. D. C. Craig, 2013: Rotating shallow water turbulence: Experiments with altimetry. *Phys. Fluids,* **25,** 106603, doi:10.1063/1.4826477.

Bastin, M. E., and P. L. Read, 1997: A laboratory study of baroclinic waves and turbulence in an internally heated rotating fluid annulus with sloping endwalls. *J. Fluid Mech.,* **339,** 173–198, doi:10.1017/S0022112097005259.

——, and ——, 1998: Experiments on the structure of baroclinic waves and zonal jets in an internally heated, rotating, cylinder of fluid. *Phys. Fluids,* **10,** 374–389, doi:10.1063/1.869530.

Berloff, P., I. Kamenkovich, and J. Pedlosky, 2009: A model of multiple zonal jets in the oceans: Dynamical and kinematical analysis. *J. Phys. Oceanogr.,* **39,** 2711–2734, doi:10.1175/2009JPO4093.1.

Boland, E. J. D., A. F. Thompson, E. Shuckburgh, and P. H. Haynes, 2012: The formation of nonzonal jets over sloped topography. *J. Phys. Oceanogr.,* **42,** 1635–1651, doi:10.1175/JPO-D-11-0152.1.

Buzyna, G., R. L. Pfeffer, and R. Kung, 1984: Transition to geostrophic turbulence in a rotating differentially heated

annulus of fluid. *J. Fluid Mech.,* **145,** 377–403, doi:10.1017/S0022112084002974.

Callies, J., and R. Ferrari, 2013: Interpreting energy and tracer spectra of upper-ocean turbulence in the submesoscale range (1200 km). *J. Phys. Oceanogr.,* **43,** 2456–2474, doi:10.1175/JPO-D-13-063.1.

Chekhlov, A., S. A. Orszag, S. Sukoriansky, B. Galperin, and I. Staroselsky, 1996: The effect of small-scale forcing on large-scale structures in two-dimensional flows. *Physica D,* **98,** 321–334, doi:10.1016/0167-2789(96)00102-9.

Condie, S. A., and P. B. Rhines, 1994: Topographic Hadley cells. *J. Fluid Mech.,* **280,** 349–368, doi:10.1017/S002211209400296X.

Cunningham, S. A., S. G. Alderson, B. A. King, and M. A. Brandon, 2003: Transport and variability of the Antarctic Circumpolar Current in Drake Passage. *J. Geophys. Res.,* **108,** 8084, doi:10.1029/2001JC001147.

Di Nitto, G., S. Espa, and A. Cenedese, 2013a: Simulating zonation in geophysical flows by laboratory experiments. *Phys. Fluids,* **25,** 086602, doi:10.1063/1.4817540.

——, ——, and ——, 2013b: Zonal jets in rotating shallow water turbulence. *Earth Sci.,* **2,** 23–30, doi:10.11648/j.earth.20130202.11.

Dritschel, D. G., and R. K. Scott, 2011: Jet sharpening by turbulent mixing. *Philos. Trans. Roy. Soc. London,* **A369,** 754–770, doi:10.1098/rsta.2010.0306.

Gage, K., and G. Nastrom, 1986: Theoretical interpretation of atmospheric wavenumber spectra of wind and temperature observed by commercial aircraft during GASP. *J. Atmos. Sci.,* **43,** 729–740, doi:10.1175/1520-0469(1986)043<0729:TIOAWS>2.0.CO;2.

Galperin, B., H. Nakano, H.-P. Huang, and S. Sukoriansky, 2004: The ubiquitous zonal jets in the atmospheres of giant planets and Earth's oceans. *Geophys. Res. Lett.,* **31,** L13303, doi:10.1029/2004GL019691.

——, S. Sukoriansky, N. Dikovskaya, P. L. Read, Y. H. Yamazaki, and R. D. Wordsworth, 2006: Anisotropic turbulence and zonal jets in rotating flows with a β-effect. *Nonlinear Processes Geophys.,* **13,** 83–98, doi:10.5194/npg-13-83-2006.

——, ——, and ——, 2010: Geophysical flows with anisotropic turbulence and dispersive waves: Flows with a β-effect. *Ocean Dyn.,* **60,** 427–441, doi:10.1007/s10236-010-0278-2.

Herbei, R., I. W. McKeague, and K. G. Speer, 2008: Gyres and jets: Inversion of tracer data for ocean circulation structure. *J. Phys. Oceanogr.,* **38,** 1180–1202, doi:10.1175/2007JPO3835.1.

Hide, R., 1958: An experimental study of thermal convection in a rotating liquid. *Philos. Trans. Roy. Soc. London,* **A250,** 441–478, doi:10.1098/rsta.1958.0004.

——, and P. J. Mason, 1970: Baroclinic waves in a rotating fluid subject to internal heating. *Philos. Trans. Roy. Soc. London,* **A268,** 201–232, doi:10.1098/rsta.1970.0073.

——, and ——, 1975: Sloping convection in a rotating fluid. *Adv. Phys.,* **24,** 47–100, doi:10.1080/00018737500101371.

Hignett, P., A. A. White, R. D. Carter, W. D. N. Jackson, and R. M. Small, 1985: A comparison of laboratory measurements and numerical simulations of baroclinic wave flows in a rotating cylindrical annulus. *Quart. J. Roy. Meteor. Soc.,* **111,** 131–154, doi:10.1002/qj.49711146705.

Hogg, A. M., and R. W. Griffiths, 2010: A coupled ocean–atmosphere laboratory model of the Antarctic Circumpolar Current. *Ocean Modell.,* **35,** 54–66, doi:10.1016/j.ocemod.2010.06.004.

Holbrook, W. S., 2005: Ocean internal wave spectra inferred from seismic reflection transects. *Geophys. Res. Lett.,* **32,** L15604, doi:10.1029/2005GL023733.

Huang, H.-P., B. Galperin, and S. Sukoriansky, 2001: Anisotropic spectra in two-dimensional turbulence on the surface of a rotating sphere. *Phys. Fluids,* **13,** 225–240, doi:10.1063/1.1327594.

Ketchum, C. B., 1972: An experimental study of baroclinic annulus waves at large Taylor number. *J. Atmos. Sci.,* **29,** 665–679, doi:10.1175/1520-0469(1972)029<0665:AESOBA>2.0.CO;2.

Klymak, J. M., and J. N. Moum, 2007: Oceanic isopycnal slope spectra. Part II: Turbulence. *J. Phys. Oceanogr.,* **37,** 1232–1245, doi:10.1175/JPO3074.1.

LaCasce, J. H., and K. H. Brink, 2000: Geostrophic turbulence over a slope. *J. Phys. Oceanogr.,* **30,** 1305–1324, doi:10.1175/1520-0485(2000)030<1305:GTOAS>2.0.CO;2.

Lappa, M., 2012: *Rotating Thermal Flows in Natural and Industrial Processes.* John Wiley and Sons, 544 pp.

Maher, N., 2010: A laboratory investigation into the effects of westerly wind stress and buoyancy forcing on the Antarctic Circumpolar Current. B.S. thesis, Research School of Earth Sciences, Australian National University, 66 pp.

Mason, P. J., 1975: Baroclinic waves in a container with sloping end walls. *Philos. Trans. Roy. Soc. London,* **A278,** 397–445, doi:10.1098/rsta.1975.0032.

Mcintyre, M. E., 2008: Potential-vorticity inversion and the wave-turbulence jigsaw: Some recent clarifications. *Adv. Geosci.,* **15,** 47–56, doi:10.5194/adgeo-15-47-2008.

Merminod, S., 2011: An exploration of the effects of mechanical forcing and buoyancy forcing on the Antarctic Circumpolar Current. Ecole Normale Superieure, Stage long de recherche, 33 pp.

Nakano, H., and N. Suginohara, 2002: A series of middepth zonal flows in the Pacific driven by winds. *J. Phys. Oceanogr.,* **32,** 161–176, doi:10.1175/1520-0485(2002)032<0161:ASOMZF>2.0.CO;2.

Ohlsen, D. R., and P. B. Rhines, 1997: Laboratory studies of equatorially trapped waves using ferrofluid. *J. Fluid Mech.,* **338,** 35–58, doi:10.1017/S0022112096004776.

Okuno, A., and A. Masuda, 2003: Effect of horizontal divergence on the geostrophic turbulence on a beta-plane: Suppression of the Rhines effect. *Phys. Fluids,* **15,** 56, doi:10.1063/1.1524188.

Orsi, A., T. Whitworth, and W. Nowlin, 1995: On the meridional extent and fronts of the Antarctic Circumpolar Current. *Deep-Sea Res. I,* **42,** 641–673, doi:10.1016/0967-0637(95)00021-W.

Panetta, R., 1993: Zonal jets in wide baroclinically unstable regions: Persistence and scale selection. *J. Atmos. Sci.,* **50,** 2073–2106, doi:10.1175/1520-0469(1993)050<2073:ZJIWBU>2.0.CO;2.

Pfeffer, R. L., G. Buzyna, and W. W. Fowlis, 1974: Synoptic features and energetics of wave-amplitude vacillation in a rotating, differentially-heated fluid. *J. Atmos. Sci.,* **31,** 622–645, doi:10.1175/1520-0469(1974)031<0622:SFAEOW>2.0.CO;2.

——, ——, and R. Kung, 1980a: Relationships among eddy fluxes of heat eddy temperature variances and basic state temperature parameters in thermally driven rotating fluids. *J. Atmos. Sci.,* **37,** 2577–2599, doi:10.1175/1520-0469(1980)037<2577:RAEFOH>2.0.CO;2.

——, ——, and ——, 1980b: Time-dependent modes of behavior of thermally driven rotating fluids. *J. Atmos. Sci.,* **37,** 2129–2149, doi:10.1175/1520-0469(1980)037<2129:TDMOBO>2.0.CO;2.

Read, P. L., 1985: Finite-amplitude, neutral baroclinic eddies and mean flows in an internally heated rotating fluid: 1. Numerical simulations and quasi-geostrophic free modes. *Dyn. Atmos. Oceans,* **9,** 135–207, doi:10.1016/0377-0265(85)90003-X.

——, 2001: Transition to geostrophic turbulence in the laboratory, and as a paradigm in atmospheres and oceans. *Surv. Geophys.,* **22,** 265–317, doi:10.1023/A:1013790802740.

——, 2005: From mixing to geostrophy: Geostrophic turbulence in atmospheres, oceans, and the laboratory. *Marine Turbulence: Theories, Observations, and Models,* H. Z. Baumert, J. H. Simpson, and J. Sundermann, Eds., Cambridge University Press, 406–422.

——, Y. H. Yamazaki, S. R. Lewis, P. D. Williams, K. Miki-Yamazaki, J. Sommeria, H. Didelle, and A. Fincham, 2004: Jupiter's and Saturn's convectively driven banded jets in the laboratory. *Geophys. Res. Lett.,* **31,** L22701, doi:10.1029/2004GL020106.

——, ——, ——, ——, R. Wordsworth, K. Miki-Yamazaki, J. Sommeria, and H. Didelle, 2007: Dynamics of convectively driven banded jets in the laboratory. *J. Atmos. Sci.,* **64,** 4031–4052, doi:10.1175/2007JAS2219.1.

Rhines, P. B., 1975: Waves and turbulence on a beta-plane. *J. Fluid Mech.,* **69,** 417–443, doi:10.1017/S0022112075001504.

——, 1994: Jets. *Chaos,* **4,** 313–339, doi:10.1063/1.166011.

Saito, I., and K. Ishioka, 2013: Angular distribution of energy spectrum in two-dimensional β-plane turbulence in the long-wave limit. *Phys. Fluids,* **25,** 076602, doi:10.1063/1.4813808.

Salmon, R., 1978: Two-layer quasi-geostrophic turbulence in a simple special case. *Geophys. Astrophys. Fluid Dyn.,* **10,** 25–52, doi:10.1080/03091927808242628.

——, 1980: Geostrophic turbulence. *Topics in Ocean Physics,* A. Osborn and P. Malanotte-Rizzoli, Eds., North-Holland, 30–78.

——, 1998: *Lectures on Geophysical Fluid Dynamics.* Oxford University Press, 378 pp.

Scott, R. K., and D. G. Dritschel, 2012: The structure of zonal jets in geostrophic turbulence. *J. Fluid Mech.,* **711,** 576–598, doi:10.1017/jfm.2012.410.

——, and A.-S. Tissier, 2012: The generation of zonal jets by large-scale mixing. *Phys. Fluids,* **24,** 126601, doi:10.1063/1.4771991.

Sinha, B., and K. Richards, 1999: Jet structure and scaling in Southern Ocean models. *J. Phys. Oceanogr.,* **29,** 1143–1155, doi:10.1175/1520-0485(1999)029<1143:JSASIS>2.0.CO;2.

Slavin, A. G., and Y. D. Afanasyev, 2012: Multiple zonal jets on the polar beta plane. *Phys. Fluids,* **24,** 016603, doi:10.1063/1.3678017.

Smith, K. S., and G. K. Vallis, 2001: The scales and equilibration of midocean eddies: Freely evolving flow. *J. Phys. Oceanogr.,* **31,** 554–571, doi:10.1175/1520-0485(2001)031<0554:TSAEOM>2.0.CO;2.

Sokolov, S., and S. R. Rintoul, 2007: Multiple jets of the Antarctic Circumpolar Current south of Australia. *J. Phys. Oceanogr.,* **37,** 1394–1412, doi:10.1175/JPO3111.1.

——, and ——, 2009: Circumpolar structure and distribution of the Antarctic Circumpolar Current fronts: 1. Mean circumpolar paths. *J. Geophys. Res.,* **114,** C11018, doi:10.1029/2008JC005108.

Sommeria, J., 1991: Experiments on vortices and Rossby waves in eastward and westward jets. *Nonlinear Topics in Ocean Physics,* A. R. Osborne, Ed., North-Holland, 227–269.

——, S. Meyers, and H. Swinney, 1989: Laboratory model of a planetary eastward jet. *Nature,* **337,** 58–61, doi:10.1038/337058a0.

Spall, M. A., 2013: Dense water formation around islands. *J. Geophys. Res. Oceans,* **118,** 2507–2519, doi:10.1002/jgrc.20185.

Sukoriansky, S., B. Galperin, and N. Dikovskaya, 2002: Universal spectrum of two-dimensional turbulence on a rotating sphere and some basic features of atmospheric circulation on giant planets. *Phys. Rev. Lett.,* **89,** 124501, doi:10.1103/PhysRevLett.89.124501.

——, N. Dikovskaya, and B. Galperin, 2007: On the arrest of inverse energy cascade and the Rhines scale. *J. Atmos. Sci.,* **64,** 3312–3327, doi:10.1175/JAS4013.1.

Thielicke, W., 2014: The flapping flight of birds–Analysis and application. Ph.D. Thesis, Rijksuniversiteit Groningen.

——, and E. J. Stamhuis, 2010: PIVlab version 1.32. MATLAB. [Available online at http://pivlab.blogspot.com/.]

Treguier, A. M., and R. L. Panetta, 1994: Multiple zonal jets in a quasigeostrophic model of the Antarctic Circumpolar Current. *J. Phys. Oceanogr.,* **24,** 2263–2277, doi:10.1175/1520-0485(1994)024<2263:MZJIAQ>2.0.CO;2.

——, N. M. Hogg, M. E. Maltrud, K. G. Speer, and V. Thierry, 2003: The origin of deep zonal flows in the Brazil basin. *J. Phys. Oceanogr.,* **33,** 580–599, doi:10.1175/1520-0485(2003)033<0580:TOODZF>2.0.CO;2.

Vallis, G. K., 2006: *Atmospheric and Oceanic Fluid Dynamics: Fundamentals and Large-Scale Circulation.* Cambridge University Press, 745 pp.

——, and M. E. Maltrud, 1993: Generation of mean flows and jets on a beta plane and over topography. *J. Phys. Oceanogr.,* **23,** 1346–1362, doi:10.1175/1520-0485(1993)023<1346:GOMFAJ>2.0.CO;2.

White, A., 2010: The atmosphere, the annulus and quasi-geostrophic theory. *Astron. Geophys.,* **51,** 4.24–4.27, doi:10.1111/j.1468-4004.2010.51424.x.

Williams, G. P., 1978: Planetary circulations: 1. Barotropic representation of Jovian and terrestrial turbulence. *J. Atmos. Sci.,* **35,** 1399–1426, doi:10.1175/1520-0469(1978)035<1399:PCBROJ>2.0.CO;2.

Wordsworth, R. D., 2009: Theoretical and experimental investigations of turbulent jet formation in planetary fluid dynamics. D.Phil. thesis, University of Oxford, 133 pp.

——, P. L. Read, and Y. H. Yamazaki, 2008: Turbulence, waves, and jets in a differentially heated rotating annulus experiment. *Phys. Fluids,* **20,** 126602, doi:10.1063/1.2990042.

Xu, Y., and L.-L. Fu, 2011: Global Variability of the wavenumber spectrum of oceanic mesoscale turbulence. *J. Phys. Oceanogr.,* **41,** 802–809, doi:10.1175/2010JPO4558.1.

Zhang, Y., and Y. Afanasyev, 2014: Beta-plane turbulence: Experiments with altimetry. *Phys. Fluids,* **26,** 026602, doi:10.1063/1.4864339.